

# A Charge-Noise Insensitive Chiral Photonic Interface for Waveguide Circuit QED

Yu-Xiang Zhang,<sup>1,\*</sup> Carles R. i Carceller,<sup>2</sup> Morten Kjaergaard,<sup>3</sup> and Anders S. Sørensen<sup>1</sup>

<sup>1</sup>*Center for Hybrid Quantum Networks (Hy-Q), The Niels Bohr Institute,  
University of Copenhagen, Blegdamsvej 17, 2100 Copenhagen Ø, Denmark*

<sup>2</sup>*Department of Physics, Technical University of Denmark, Fysikvej 307, 2800 Kgs. Lyngby, Denmark*

<sup>3</sup>*Center for Quantum Devices, Niels Bohr Institute,  
University of Copenhagen, 2100 Copenhagen Ø, Denmark*

(Dated: March 9, 2022)

A chiral photonic interface is a quantum system that has different probabilities for emitting photons to the left and right. An on-chip compatible chiral interface is attractive for both fundamental studies of light-matter interactions and applications to quantum information processing. We propose such a chiral interface based on superconducting circuits, which has wide bandwidth, rich tunability, and high tolerance to fabrication variations. The proposed interface consists of a core that uses Cooper-pair-boxes (CPBs) to break time-reversal symmetry, and two superconducting transmons which connect the core to a waveguide in the manner reminiscent of a “giant atom”. The transmons form a state decoupled from the core, akin to dark state of atomic physics, rendering the whole interface insensitive to the CPB charge noise. The proposed interface can be extended to realize a broadband fully passive on-chip circulator for microwave photons.

The emission of photons from quantum systems is typically non-chiral, meaning that the emitted photons have equal probability to propagate in opposite directions. The opposite situation, where the emitted photons propagate in a single direction, allows for a wide range of novel phenomena including cascaded driven-dissipative dynamics [1, 2], spin dimers [3, 4], photonic bound states [5–7], and solvable models of chiral waveguide quantum electrodynamics (QED) [8]. Chiral interfaces enabling the study of such effects have recently been developed for optical photons [9], but optical systems are prone to losses, limiting the quality of the interfaces. In comparison, superconducting circuits have almost ideal interfaces to guided microwave photons [10, 11], potentially allowing for much cleaner demonstrations of these fundamental effects.

Chiral interfaces to superconducting systems are also of immense technological interest. Scaling superconducting quantum computers to larger sizes puts high demands on the ability to route signals between different components on the chips, e.g., using circulators. Such circulators necessarily break Lorentz reciprocity and thereby time-reversal symmetry (TRS). Commercially available circulators often exploit the Faraday effect [12]. However, such components are off-chip, requiring additional space inside the experimental apparatus. Most of the existing proposals for on-chip circulators break TRS by tailored active control [13–23], e.g., via a synthetic magnetic field [22], or by dynamically modulating switches and delays [23]. On-chip circulators that can be operated in a passive form, thereby simplifying its experimental implementations, however remain elusive. A Josephson junction ring threaded by a constant magnetic flux breaks TRS [24], but its applicability as a circulator in current superconducting hardware is limited, because the system must be operated in the Cooper-pair-box (CPB)

regime [24–27] which is susceptible to charge noise [11, 28] and only attains a narrow bandwidth. In this Letter, we develop an on-chip tunable broadband charge-insensitive chiral system, based on CPBs and superconducting transmon qubits. The interface can directly be extended to realise a circulator for routing signals in large scale superconducting devices. Recent related proposals have used delicate qubit degeneracy and interference to realize unidirectional interactions without breaking TRS thus not allowing them to be used as a circulator [29, 30].

The proposed circuit is illustrated in Fig. 1(a). It has a core composed of two CPBs and an applied external flux (green box). When connected at two separated locations on the waveguide, the system is reminiscent of a “giant atom” [31–33]. This core in itself already provides a chiral interface, albeit limited by bandwidth, fabrication variations, and charge noise [34]. Introducing two flux-tunable transmons as mediators between CPBs and the waveguide addresses all these issues. Similar coupling schemes have previously been considered with microwave resonators [27], but transmons allow for stronger spatial confinement of excitations, and thereby larger couplings to the CPBs, while simultaneously maintaining sizable coupling to waveguides. Furthermore, by operating in a particular dark state configuration [35] we show that excitation of the CPBs can be suppressed, such that the interface maintains the excellent coherence properties of transmons [36, 37], while still exploiting the inherent breaking of TRS by the CPBs. Finally the tunability of our chiral interface allows compensating fabrication variations as well as control of the operating frequency.

*Preliminaries.* We first consider two coupled CPBs, “a” and “b”, which as a whole, has the ground state  $|g_{ab}\rangle$  and a non-degenerate excited state  $|e\rangle$ . The transition between them is resonant with waveguide modes of wavenumber  $\pm k_0$ . We couple CPB-a and CPB-b to

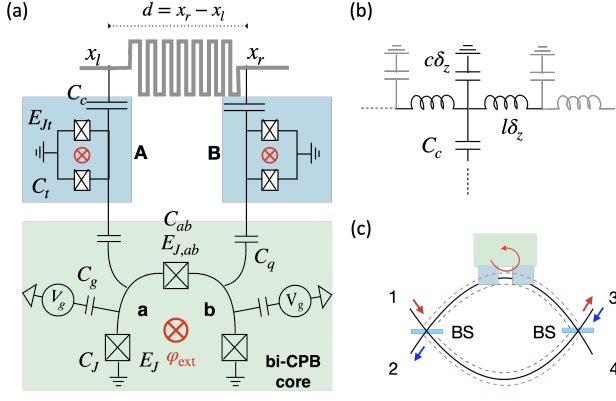


Figure 1. Proposal for realizing on-chip compatible charge-noise insensitive chiral photonic interface. (a) Circuit of the chiral interface consisting of two CPBs (green boxes) coupled to a waveguide (top) through two tunable transmons (blue boxes) connecting to the waveguide at positions  $x_l$  and  $x_r$ .  $C_J$  and  $E_J$  denotes the capacitance and Josephson energy of the CPBs,  $C_{ab}$  and  $E_{J,ab}$  are those of the junction connecting CPB-a and CPB-b,  $\varphi_{\text{ext}}$  is the dimensionless external flux,  $C_g$  is the gate capacitance,  $C_q$  couples the CPB and transmons,  $C_t$  and  $E_{J_t}$  are the total capacitance and Josephson energy (tunable) of the transmon and  $C_c$  couples the transmons to the transmission line. (b) Circuit model of the capacitive coupling between a transmon and the transmission line. (c) A circulator based on chiral interface (right-hand chirality) and Mach-Zehnder interferometer. “BS” denotes 50:50 beam splitters. Input from port-1 goes to port-3 while input from port-3 goes to port-2.

the waveguide at positions  $x_l$  and  $x_r$ , respectively [see Fig. 1(a)], resulting in coupling operators of the form  $\hat{a}_{\pm k_0}(\hat{n}_a + e^{\pm i k_0 d} \hat{n}_b)$ , where  $\hat{a}_{\pm k_0}$  is the photon annihilation operator,  $d = x_r - x_l$  and  $\hat{n}_{a/b}$  is the CPB charge number operator. Within the rotating-wave approximation and perturbation theory, the decay from  $|e\rangle$  to

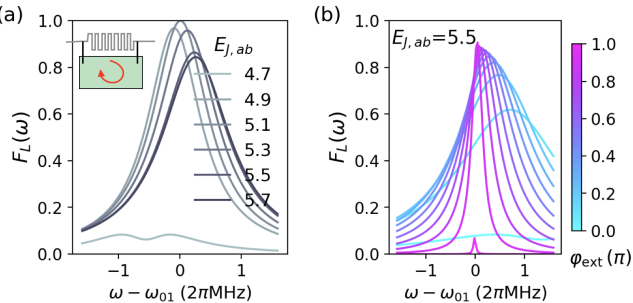


Figure 2. Fidelity of circulator  $F_L(\omega)$  against the detuning to the first excited state for direct coupling between the waveguide and the bi-CPB core. The device parameters are:  $c\delta_z = C_q = C_\Sigma = C_{ab} = 1\text{fF}$ ,  $E_J = 5.5\text{ hGHz}$ , and (a)  $\varphi_{\text{ext}} = 0.5\pi$  and various values of  $E_{J,ab}(\text{hGHz})$ ; (b)  $E_{J,ab} = 5.5\text{ hGHz}$  and the external flux  $\varphi_{\text{ext}}$  varying from 0 to  $\pi$ .

left/right going photons depends on the magnitude of

$$\lambda_{\pm} = \eta_a + e^{\pm i k_0 d} \eta_b, \quad \eta_{a/b} = \langle e | \hat{n}_{a/b} | g_{ab} \rangle. \quad (1)$$

This formula expresses the interference between excitation decaying through the left and right arms in Fig. 2(a), which depends on both the coupling matrix element  $\eta_{a/b}$  at  $x_l/r$  and the phase  $e^{\pm i k_0 d}$  from waveguide propagation between them.

A chiral interface with a single excited state requires TRS to be broken since left and right propagation are connected by TRS, and a state invariant under TRS cannot distinguish these two possibilities. Breaking of TRS, however, may induce a phase difference between  $\eta_a$  and  $\eta_b$  allowing the cancellation of  $\lambda_+$  or  $\lambda_-$  for a suitable  $k_0 d$  if  $|\eta_a| = |\eta_b|$ .

Incorporating the chiral interface into one of the arms of a balanced Mach-Zehnder interferometer enables the construction of a four-port photonic circulator [Fig. 1(c)]. Suppose the scattering matrix of the chiral interface is  $S_{\epsilon\epsilon'}(\omega_k)$  with  $\epsilon, \epsilon' = \pm 1$  denoting the matrix element from wavenumber  $\epsilon'k$  to  $\epsilon k$ . If the interface has ideal right-hand chirality, there will be no phase shift for the uncoupled left-moving photons ( $S_{--} = 1$ ), whereas a  $\pi$  phase shift is attained for the perfectly coupled right-moving photons ( $S_{++} = -1$ ). This phase difference of  $\pi$  implies that the Mach-Zehnder interferometer, shown in Fig. 1(c), can be balanced such that a right-moving photon incident in Port-1 exits through Port-3, whereas a left-moving photon incident in Port-3 exits through Port-2, realizing a circulator. We define the fidelity of the circulator as the probability for these two inputs to exit through the correct port, which is given by

$$F_{R/L}(\omega) = \frac{1}{16} |1 \mp S_{++}(\omega)|^2 |1 \pm S_{--}(\omega)|^2. \quad (2)$$

Obviously  $F_{R/L} = 1$  if  $S_{++} = \mp 1$  and  $S_{--} = \pm 1$ . In the Supplemental Material [38] we show the system Hamiltonian and use the input-output formalism to derive the scattering matrix, based on which the fidelity (2) can be numerically evaluated.

*The bi-CPB core.* TRS can be broken by Josephson junction rings threaded by magnetic flux [24]. Here we use an equivalent construction [38] depicted in the green box of Fig. 1(a). It consists of two CPBs denoted by “a” and “b” and a constant external magnetic flux. We refer to that as the “bi-CPB core”. For now the two CPBs are assumed to have identical parameters. Each CPB has a junction with Josephson energy  $E_J$  and capacitance  $C_J$ . The voltage source determines the offset charge  $n_{g,a/b}$  through a capacitor with capacitance  $C_g$ . We define  $C_\Sigma = C_J + C_g$ . The two CPBs are connected by a Josephson junction with capacitance  $C_{ab}$  and Josephson energy  $E_{J,ab}$ . The external flux  $\varphi_{\text{ext}}$  is made dimensionless by expressing it in units of  $\Phi_0/(2\pi)$  with  $\Phi_0$  being the flux quantum. As depicted in Fig. 1(b),

the transmission line waveguide is modeled by an infinite chain of coupled LC-oscillators with capacitance  $c\delta_z$  and inductance  $l\delta_z$ . The waveguide parameters are set by realistic impedance  $Z = \sqrt{l/c} = 50\Omega$  and the speed of light  $v_g = 1/\sqrt{lc} \approx 1.2 \times 10^8 \text{m/s}$ . The elementary length,  $\delta_z$ , is determined by the lateral size of the coupling capacitor  $C_c$  (or  $C_q$  if using only the bi-CPB core).

At first, we consider coupling the bi-CPB core directly to the waveguide at  $x_{l/r}$ , with device parameters given in the caption of Fig. 2. Particularly, we set  $c\delta_z = 1\text{fF}$  corresponding to  $\delta_z \approx 5\mu\text{m}$ , which is comparable to the size of typical CPBs [25]. To suppress the dephasing caused by charge noise, the offset charge  $n_{g,a/b}$  is fixed at the “sweet spot” where  $\partial\omega_{01}/\partial n_g = 0$  [39] and  $\omega_{01}$  is the energy gap between the first excited state and the ground state of the core (the sweet spot  $n_{g,a/b} = 0.5$  must be excluded, because here particle-hole symmetry preserves TRS). The separation  $d = x_r - x_l$  is selected so that  $k_0 d = \pi/2$ .

In Fig. 2(a), we plot  $F_L(\omega)$  as a function of detuning from  $\omega_{01}$  for  $\varphi_{\text{ext}} = 0.5\pi$  and a few values of  $E_{J,ab}$ . The plot shows that the bare core can indeed acts as a chiral emitter. As evident from Fig. 2(a) this configuration of the chiral interface suffer from several shortcomings. Firstly, the peak fidelity,  $\max_{\omega} F_{R/L}(\omega)$ , is sensitive to the exact value of  $E_{J,ab}$ , leaving the device performance highly sensitive to fabrication variation. Fabrication variations might be compensated by adapting the tunable flux  $\varphi_{\text{ext}}$ . To examine this, we choose a representative  $E_{J,ab} = 5.5 \text{ hGHz}$  corresponding to a 10% deviation from the ideal value and plot  $F_L(\omega)$  as a function of  $\varphi_{\text{ext}}$  in Fig. 2(b). It shows that this tuning fails to make the maximal fidelity above 0.9. Furthermore, tuning  $\varphi_{\text{ext}}$  changes  $\omega_{01}$ , rendering this configuration inadequate for tasks where photon frequencies are fixed. Figure 2 also shows that the bandwidth is less than 1MHz, which severely limits the functionality.

*The transmon-coupled bi-CPB chiral photonic interface.* The bandwidth is limited by the weak interaction between the small CPBs and the waveguide excitations delocalized in wavelength scale. To overcome it, we propose to insert transmons between the bi-CPB core and the waveguide, as shown in Fig. 1(a). These transmons, which have lateral size in between the CPBs and the photonic wavelength, act as efficient mediators. In Fig. 3(a) we plot  $F_{R/L}(\omega)$  as a function of the detuning to the first two excited states ( $\omega_{01}$  and  $\omega_{02}$ ) for the CPB-transmon-coupled system. The device parameters used in the calculation are listed in Fig. 3(c), which are chosen based on experiment-relevant considerations but not optimized. Particularly, we have taken  $c\delta_z = 50\text{fF}$  i.e.,  $\delta_z \approx 250\mu\text{m}$ , corresponding to the lateral size of the transmon reported in Ref. [40]. Figure 3(a) shows that the bandwidth is significantly improved. However, while a left-hand chirality ( $F_L \gg F_R$ ) is realized for  $\omega \approx \omega_{01}$  (and  $\omega \approx \omega_{03}$ ) – similarly to the bare bi-CPB core – we observe the opposite

chirality for  $\omega \approx \omega_{02}$  ( $F_R \gg F_L$ ). This feature indicates the distinctness of the 2nd excited state. Below we use an approximate model to highlight multiple benefits brought by this state.

We assume that the two transmons, indexed by “A” and “B” in Fig. 1(a), are identical in parameters, and consider a restricted Hilbert space spanned by the ground state and the singly-excited states of either transmon-A,B, or the bi-CPB core, which will be denoted by  $|1_A\rangle$ ,  $|1_B\rangle$ , and  $|e\rangle$ , respectively. The device Hamiltonian reads  $H = H_0 + H_{\text{int}}$ , where  $H_0 = e_1 |e\rangle\langle e| + \omega_t(|1_A\rangle\langle 1_A| + |1_B\rangle\langle 1_B|)$  with  $e_1$  and  $\omega_t$  the energies of the 1st excited states of the core and the transmons, respectively. The interaction Hamiltonian is

$$H_{\text{int}} = g\hat{n}_A(\hat{n}_a - n_{g,a}) + g\hat{n}_B(\hat{n}_b - n_{g,b}), \quad (3)$$

where  $g$  is the coupling strength. Using rotating-wave approximation upon  $H_{\text{int}}$ , and restricting it to the reduced Hilbert space, we rewrite  $H$  as

$$H = H_0 + \tilde{g}(|\psi_c\rangle\langle e| + |e\rangle\langle\psi_c|), \quad (4)$$

where  $\tilde{g}$  is modified from  $g$  and

$$|\psi_c\rangle \propto \eta_a^* |1_A\rangle + \eta_b^* |1_B\rangle, \quad (5)$$

with  $\eta_{a(b)} = \langle e|\hat{n}_{a(b)}|g_{ab}\rangle$  as in Eq. (1). The coupling between  $|\psi_c\rangle$  and  $|e\rangle$  yields the 1st excited state  $|\Psi\rangle$

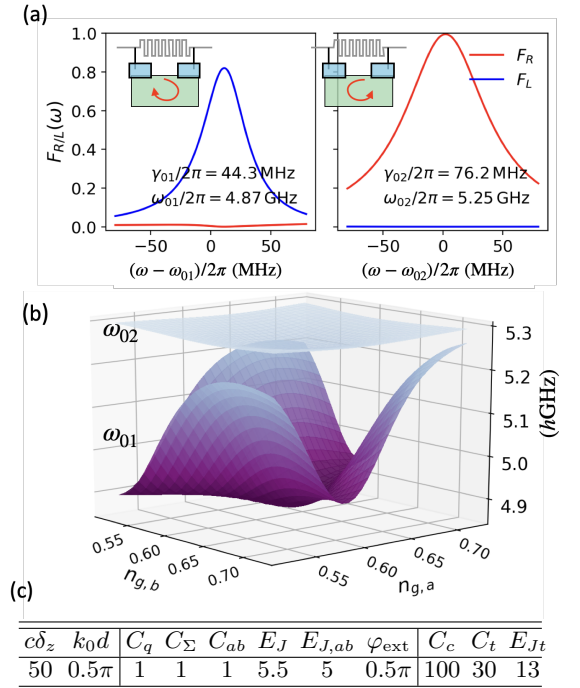


Figure 3. Energy levels and performance of the full system. (a) Fidelity of circulator as a function of the detuning from  $\omega_{01}$  and  $\omega_{02}$  with device parameters in (c). (b) Values (in unit of hGHz) of  $\omega_{01}$  and  $\omega_{02}$  of the full device as a function of  $n_{g,a/b}$ , using parameters listed in (c), where units for capacitances and Josephson energies are fF and hGHz, respectively.

with energy  $\omega_{01} = e_1 + \Delta_-$  and the 3rd excited state  $|\Psi_+\rangle$  with energy  $\omega_{03} = e_1 + \Delta_+$ ,

$$|\Psi_\pm\rangle \propto \underbrace{\Delta_\pm |\psi_c\rangle}_{\text{transmons}} + \underbrace{i\tilde{g} |e\rangle}_{\text{bi-CPB}} \quad (6)$$

where  $\Delta_\pm = -\delta/2 \pm \sqrt{\delta^2/4 + \tilde{g}^2}$  with  $\delta = e_1 - \omega_t$ . The 2nd excited state is a so-called dark state [35], which has no excitation on the core,

$$|\Psi_{\text{de}}\rangle \propto \eta_b |1_A\rangle - \eta_a |1_B\rangle. \quad (7)$$

Despite being decoupled,  $|\Psi_{\text{de}}\rangle$  still attains chiral property from the core. The constants  $\eta_{a(b)}$ , however, have different orders and signs in  $|\Psi_{\text{de}}\rangle$  and  $|\psi_c\rangle$ , which lead to opposite chirality.

A more important observation is that the state  $|\Psi_{\text{de}}\rangle$  does not contain the bi-CPB state  $|e\rangle$ . Thus, it is not affected by the CPB charge noise and keeps the charge noise insensitivity of the transmon qubits [28]. To illustrate this, Fig. 3(b) shows  $\omega_{01}$  and  $\omega_{02}$  as a function of the offset charges  $n_{g,a/b}$ . The results are numerically evaluated from the complete Hamiltonian (see [38] for details) using device parameters listed in Fig. 3(c). Figure 3(b) demonstrates that  $\omega_{02}$  is significantly more stable than  $\omega_{01}$ . The fluctuation of  $\omega_{02}$  does not exceed its linewidth  $\gamma_{02}/2\pi \approx 76$  MHz despite the large variations in  $n_{g,a/b}$ . Thus, the offset charges  $n_{g,a(b)}$  need not be at the sweet spots, and can be used as control knobs to provide tunability.

*Tunability of the chiral interface.* First, we demonstrate that by tuning  $n_{g,a/b}$  and  $\varphi_{\text{ext}}$  we can address issues of fabrication variation in the device parameters. To simulate realistic fabrication variations, we sample values of capacitance and CPB Josephson energy uniformly in intervals bounded by  $\pm 1\%$  and  $\pm 10\%$ , respectively, from the intended values listed in Fig. 3(c). The transmon Josephson energy  $E_{Jt}$  is fixed at the intended values because they can be tuned *in situ* via flux-control. We collect 150 such “realistic samples”, which includes cases with asymmetries between CPB-a and CPB-b, and between transmon-A and transmon-B. In Fig. 4(a), we fix  $n_{g,a/b}$  and  $\varphi_{\text{ext}}$  at the optimal value for the ideal parameters, and show by grey points their individual maximal fidelity (vertical coordinate), frequency where the maximal fidelity is obtained (horizontal coordinate), and the  $F_{R/L} > 0.9$  bandwidth (horizontal error bar). While the performance is generally good, certain instances with poor chiral fidelity are observed. Next, for each sample that has a maximal fidelity less than 0.99, we search for values of  $n_{g,a/b}$  and  $\varphi_{\text{ext}}$  that improve the performance. The red points in Fig. 4(a) show the result of such optimization. We are always able to tune the maximal fidelity above 0.99. Additional details about how the maximal fidelity and bandwidth depend on  $n_{g,a/b}$  and  $\varphi_{\text{ext}}$  are given in the Supplemental Material [38].

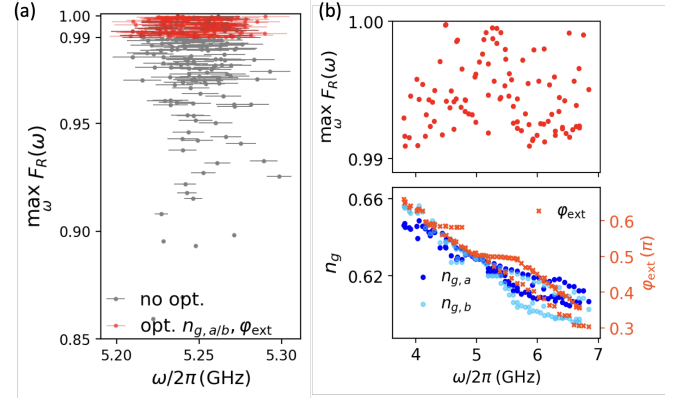


Figure 4. Tunability of the chiral interface. (a) 150 realizations of the chiral interfaces with device parameters randomly sampled to represent fabrication variations (see text for details). The marker shows peak fidelity for a given realization, error bar indicates the  $F_R > 0.9$  bandwidth. The grey points show results obtained when  $n_{g,a/b}$  and  $\varphi_{\text{ext}}$  are optimized for the ideal parameters listed in Fig. 3(c). Red points show fidelities obtained when  $n_{g,a/b}$  and  $\varphi_{\text{ext}}$  are optimized for each realization. (b) upper panel: Peak fidelities as a function of photon frequency, for the chiral interface with parameters given in Fig. 3(c) and 100 samples of transmon Josephson energy  $E_{Jt}$  between  $6 \sim 22$  hGHz. For each red dot thereof, the vertically aligned markers in the lower panel shows the adaptively optimized  $n_{g,a/b}$  and  $\varphi_{\text{ext}}$ .

Additionally, flux-tunable transmons [28] enables tuning of the operating frequency of our device. We consider the parameters listed in Fig. 3(c) (including the separation  $d$ ). For 100 values of  $E_{Jt}$  between  $6 \sim 22$  hGHz, we optimize the peak fidelity to be higher than 0.99 by tuning  $n_{g,a/b}$  and  $\varphi_{\text{ext}}$ . The results are presented in Fig. 4(b). It shows that for photons in a band of 3 GHz width, the same device can always be tuned to provide an excellent chiral interaction. This broad adaptability is rooted in the breaking of TRS. When we tune  $E_{Jt}$ ,  $\omega_{02}$  changes and so does the phase  $k_0 d$  with  $k_0 = \omega_{02}/v_g$ . Adjusting the flux  $\phi$ , however, allows us to achieve complete destructive interference in one of the directions. Our chiral interface thus works in principle as long as  $k_0 d \neq 0 \pmod{\pi}$ .

*Discussion and conclusion.* The bandwidth for  $F_{R/L}(\omega) > 0.9$  is about 25 MHz in Fig. 3(a). This is limited by the transmon decay rate, which is typically on the order of 100 MHz. The bandwidth can thus be directly enhanced by designing transmons with larger decay rates. We note however that as the decay rate approaches roughly a tenth of the transition frequency ( $0.1\omega_0/2\pi \sim 500$  MHz) the system reaches the ultra-strong coupling regime of waveguide QED [41] requiring a more advanced theoretical description [42, 43].

Our interface relies on the 2nd excited state. This raises the concern that decay to the 1st excited state may jeopardizes the performance. This transition is negligible

for two reasons. First, the transition matrix element is tiny (vanishing in our simplified model  $\langle \Psi_- | \hat{n}_{A/B} | \Psi_{de} \rangle = 0$ ). Second, the waveguide mode density at  $\omega_{12}/2\pi = (\omega_{02} - \omega_{01})/2\pi \sim 100\text{MHz}$  is low. As a result, the decay rate to the 1st excited state is numerically found to be  $\gamma_{12}/2\pi \sim 10\text{kHz}$ , which is much smaller than  $\gamma_{02}/2\pi \sim 100\text{MHz}$ .

In conclusion, we have shown that by introducing two transmons, a passive charge-noise insensitive chiral photonic interface can be build, based on a core consisting of CPBs and an external magnetic flux that breaks TRS. The interface has rich tunability, making it tolerant to experimentally relevant fabrication variations. The bandwidth of  $F_{R/L} > 0.9$  is a few tens of MHz for realistic transmon parameters with decay rates typically around 100MHz. With tunable transmons (SQUIDS), our design can be tuned in a band as wide as a few GHz. These properties makes our chiral interface highly attractive for e.g., on chip routing of microwave signals [13–23, 29, 30] as well as fundamental studies of chiral waveguide QED [3, 4, 7, 44].

A. S. Sørensen thanks Peter Lodahl, Per Delsing and Göran Johansson for useful discussions. M. Kjaergaard gratefully acknowledges helpful and insightful discussions with Bharath Kannan. Y.-X. Zhang, M. Kjaergaard & A. S. Sørensen acknowledge financial support from the Danish National Research Foundation. M. Kjaergaard was also supported by Villum Fonden (grant 37467) through a Villum Young Investigator grant.

---

\* [iyxz@nbi.ku.dk](mailto:iyxz@nbi.ku.dk)

- [1] C. W. Gardiner, Driving a quantum system with the output field from another driven quantum system, *Phys. Rev. Lett.* **70**, 2269 (1993).
- [2] H. J. Carmichael, Quantum trajectory theory for cascaded open systems, *Phys. Rev. Lett.* **70**, 2273 (1993).
- [3] T. Ramos, H. Pichler, A. J. Daley, and P. Zoller, Quantum spin dimers from chiral dissipation in cold-atom chains, *Phys. Rev. Lett.* **113**, 237203 (2014).
- [4] I. M. Mirza and J. C. Schotland, Multiqubit entanglement in bidirectional-chiral-waveguide qed, *Phys. Rev. A* **94**, 012302 (2016).
- [5] J.-T. Shen and S. Fan, Strongly correlated multiparticle transport in one dimension through a quantum impurity, *Phys. Rev. A* **76**, 062709 (2007).
- [6] H. Zheng, D. J. Gauthier, and H. U. Baranger, Cavity-free photon blockade induced by many-body bound states, *Phys. Rev. Lett.* **107**, 223601 (2011).
- [7] S. Mahmoodian, G. Calajó, D. E. Chang, K. Hammerer, and A. S. Sørensen, Dynamics of many-body photon bound states in chiral waveguide qed, *Phys. Rev. X* **10**, 031011 (2020).
- [8] V. I. Yudson, Dynamics of integrable quantum systems, *Zh. Eksp. Teor. Fiz.* **88**, 1757 (1985).
- [9] P. Lodahl, S. Mahmoodian, S. Stobbe, A. Rauschenbeutel, P. Schneeweiss, J. Volz, H. Pichler, and P. Zoller, Chiral quantum optics, *Nature* **541**, 473 (2017).
- [10] I.-C. Hoi, C. M. Wilson, G. Johansson, T. Palomaki, B. Peropadre, and P. Delsing, Demonstration of a single-photon router in the microwave regime, *Phys. Rev. Lett.* **107**, 073601 (2011).
- [11] A. Blais, A. L. Grimsmon, S. M. Girvin, and A. Wallraff, Circuit quantum electrodynamics (2020), [arXiv:2005.12667 \[quant-ph\]](https://arxiv.org/abs/2005.12667).
- [12] C. Caloz, A. Alù, S. Tretyakov, D. Sounas, K. Achouri, and Z.-L. Deck-Léger, Electromagnetic nonreciprocity, *Phys. Rev. Applied* **10**, 047001 (2018).
- [13] K. M. Sliwa, M. Hatridge, A. Narla, S. Shankar, L. Frunzio, R. J. Schoelkopf, and M. H. Devoret, Reconfigurable josephson circulator/directional amplifier, *Phys. Rev. X* **5**, 041020 (2015).
- [14] B. Abdo, K. Sliwa, S. Shankar, M. Hatridge, L. Frunzio, R. Schoelkopf, and M. Devoret, Josephson directional amplifier for quantum measurement of superconducting circuits, *Phys. Rev. Lett.* **112**, 167701 (2014).
- [15] B. Abdo, N. T. Bronn, O. Jinka, S. Olivadese, A. D. Córcoles, V. P. Adiga, M. Brink, R. E. Lake, X. Wu, D. P. Pappas, and J. M. Chow, Active protection of a superconducting qubit with an interferometric josephson isolator, *Nature Communications* **10**, 3154 (2019).
- [16] J. Kerckhoff, K. Lalumière, B. J. Chapman, A. Blais, and K. W. Lehnert, On-chip superconducting microwave circulator from synthetic rotation, *Phys. Rev. Applied* **4**, 034002 (2015).
- [17] S. Barzanjeh, M. Wulf, M. Peruzzo, M. Kalaei, P. B. Dieterle, O. Painter, and J. M. Fink, Mechanical on-chip microwave circulator, *Nature Communications* **8**, 10.1038/s41467-017-01304-x (2017).
- [18] A. Metelmann and H. E. Türeci, Nonreciprocal signal routing in an active quantum network, *Phys. Rev. A* **97**, 043833 (2018).
- [19] I.-C. Hoi, C. M. Wilson, G. Johansson, T. Palomaki, B. Peropadre, and P. Delsing, Demonstration of a single-photon router in the microwave regime, *Phys. Rev. Lett.* **107**, 073601 (2011).
- [20] A. Kamal, J. Clarke, and M. H. Devoret, Noiseless non-reciprocity in a parametric active device, *Nature Physics* **7**, 311 (2011).
- [21] N. A. Estep, D. L. Sounas, J. Soric, and A. Alù, Magnetic-free non-reciprocity and isolation based on parametrically modulated coupled-resonator loops, *Nature Physics* **10**, 923 (2014).
- [22] P. Roushan, C. Neill, A. Megrant, Y. Chen, R. Babush, R. Barends, B. Campbell, Z. Chen, B. Chiaro, A. Dunsworth, A. Fowler, E. Jeffrey, J. Kelly, E. Lucero, J. Mutus, P. J. J. O'Malley, M. Neeley, C. Quintana, D. Sank, A. Vainsencher, J. Wenner, T. White, E. Kapit, H. Neven, and J. Martinis, Chiral ground-state currents of interacting photons in a synthetic magnetic field, *Nature Physics* **13**, 146 (2016).
- [23] B. J. Chapman, E. I. Rosenthal, and K. W. Lehnert, Design of an on-chip superconducting microwave circulator with octave bandwidth, *Phys. Rev. Applied* **11**, 044048 (2019).
- [24] J. Koch, A. A. Houck, K. L. Hur, and S. M. Girvin, Time-reversal-symmetry breaking in circuit-qed-based photon lattices, *Physical Review A* **82**, 10.1103/physreva.82.043811 (2010).
- [25] A. Wallraff, D. I. Schuster, A. Blais, L. Frunzio, R.-S. Huang, J. Majer, S. Kumar, S. M. Girvin, and R. J.

- Schoelkopf, Strong coupling of a single photon to a superconducting qubit using circuit quantum electrodynamics, *Nature* **431**, 162 (2004).
- [26] C. Müller, S. Guan, N. Vogt, J. H. Cole, and T. M. Stace, Passive on-chip superconducting circulator using a ring of tunnel junctions, *Phys. Rev. Lett.* **120**, 213602 (2018).
- [27] B. Richman and J. M. Taylor, Circulation by microwave-induced vortex transport for signal isolation (2020), [arXiv:2010.04118](https://arxiv.org/abs/2010.04118) [quant-ph].
- [28] J. Koch, T. M. Yu, J. Gambetta, A. A. Houck, D. I. Schuster, J. Majer, A. Blais, M. H. Devoret, S. M. Girvin, and R. J. Schoelkopf, Charge-insensitive qubit design derived from the cooper pair box, *Phys. Rev. A* **76**, 042319 (2007).
- [29] P.-O. Guimond, B. Vermersch, M. L. Juan, A. Sharafiev, G. Kirchmair, and P. Zoller, A unidirectional on-chip photonic interface for superconducting circuits, *npj Quantum Information* **6**, 10.1038/s41534-020-0261-9 (2020).
- [30] N. Gheeraert, S. Kono, and Y. Nakamura, Programmable directional emitter and receiver of itinerant microwave photons in a waveguide, *Phys. Rev. A* **102**, 053720 (2020).
- [31] A. Frisk Kockum, P. Delsing, and G. Johansson, Designing frequency-dependent relaxation rates and lamb shifts for a giant artificial atom, *Phys. Rev. A* **90**, 013837 (2014).
- [32] A. F. Kockum, Quantum optics with giant atoms – the first five years, in *International Symposium on Mathematics, Quantum Theory, and Cryptography*, edited by T. Takagi, M. Wakayama, K. Tanaka, N. Kunihiro, K. Kimoto, and Y. Ikematsu (Springer Singapore, 2021).
- [33] B. Kannan, M. J. Ruckriegel, D. L. Campbell, A. F. Kockum, J. Braumüller, D. K. Kim, M. Kjaergaard, P. Krantz, A. Melville, B. M. Niedzielski, A. Vepsäläinen, R. Winik, J. L. Yoder, F. Nori, T. P. Orlando, S. Gustavsson, and W. D. Oliver, Waveguide quantum electrodynamics with superconducting artificial giant atoms, *Nature* **583**, 775 (2020).
- [34] C. R. i Carceller, *Chiral photon interaction mediated by a superconducting circuit QED*, Master's thesis, University of Copenhagen (2020).
- [35] E. Arimondo and G. Orriols, Nonabsorbing atomic coherences by coherent two-photon transitions in a three-level optical pumping, *Lettere Al Nuovo Cimento Series 2* **17**, 333 (1976).
- [36] A. P. M. Place, L. V. H. Rodgers, P. Mundada, B. M. Smitham, M. Fitzpatrick, Z. Leng, A. Premkumar, J. Bryon, A. Vrajitoarea, S. Sussman, G. Cheng, T. Madhavan, H. K. Babla, X. H. Le, Y. Gang, B. Jäck, A. Geynis, N. Yao, R. J. Cava, N. P. de Leon, and A. A. Houck, New material platform for superconducting transmon qubits with coherence times exceeding 0.3 milliseconds, *Nature Communications* **12**, 10.1038/s41467-021-22030-5 (2021).
- [37] M. Kjaergaard, M. E. Schwartz, J. Braumüller, P. Krantz, J. I.-J. Wang, S. Gustavsson, and W. D. Oliver, Superconducting qubits: Current state of play, *Annual Review of Condensed Matter Physics* **11**, 369–395 (2020).
- [38] *Supplemental Material*.
- [39] D. Vion, Manipulating the quantum state of an electrical circuit, *Science* **296**, 886 (2002).
- [40] M. Mirhosseini, E. Kim, X. Zhang, A. Sipahigil, P. B. Dieterle, A. J. Keller, A. Asenjo-Garcia, D. E. Chang, and O. Painter, Cavity quantum electrodynamics with atom-like mirrors, *Nature* **569**, 692 (2019).
- [41] P. Forn-Díaz, J. J. García-Ripoll, B. Peropadre, J.-L. Orgiazzi, M. A. Yurtalan, R. Belyansky, C. M. Wilson, and A. Lupascu, Ultrastrong coupling of a single artificial atom to an electromagnetic continuum in the nonperturbative regime, *Nature Physics* **13**, 39 (2016).
- [42] E. Sanchez-Burillo, D. Zueco, J. J. Garcia-Ripoll, and L. Martin-Moreno, Scattering in the ultrastrong regime: Nonlinear optics with one photon, *Phys. Rev. Lett.* **113**, 263604 (2014).
- [43] T. Shi, Y. Chang, and J. J. García-Ripoll, Ultrastrong coupling few-photon scattering theory, *Phys. Rev. Lett.* **120**, 153602 (2018).
- [44] S. Mahmoodian, M. Čepulkovskis, S. Das, P. Lodahl, K. Hammerer, and A. S. Sørensen, Strongly correlated photon transport in waveguide quantum electrodynamics with weakly coupled emitters, *Phys. Rev. Lett.* **121**, 143601 (2018).

# Supplemental Material for “A Charge-Noise Insensitive Chiral Photonic Interface for Waveguide Circuit QED”

Yu-Xiang Zhang,<sup>1</sup> Carles R. i Carceller,<sup>2</sup> Morten Kjaergaard,<sup>3</sup> and Anders S. Sørensen<sup>1</sup>

<sup>1</sup>Niels Bohr Institute, University of Copenhagen, Blegdamsvej 17, 2100 Copenhagen Ø, Denmark

<sup>2</sup>Department of Physics, Technical University of Denmark, Fysikvej 307, 2800 Kgs. Lyngby, Denmark

<sup>3</sup>Niels Bohr Institute, University of Copenhagen,  
Universitetsparken 5, 2100 Copenhagen Ø, Denmark

(Dated: March 9, 2022)

This Supplemental Material is organized as follows: In Sec. **S-I**, we derive the Hamiltonians of the chiral interface and the coupling to the transmission line waveguide, and present the Hilbert space truncation used in all the numerical calculations. In Sec. **S-II**, we discuss the equivalence between our bi-CPB core and the Josephson junction ring proposed in Ref. [S1]. In Sec. **S-III**, we derive the single-photon scattering matrix of the chiral interface using the standard input-output formalism. In Sec. **S-IV**, we show data parallel to that presented in the main text, but for a different family of device parameters. In Sec. **S-V**, we calculate the maximal fidelity and bandwidth of  $F_{R/L} > 0.9$  for different values of the CPB offset charges  $n_{g,a(b)}$  and constant external flux  $\varphi_{\text{ext}}$ , in order to demonstrate that tuning  $n_{g,a(b)}$  and  $\varphi_{\text{ext}}$  is able to circumvent fabrication variation.

## S-I. THEORETICAL FORMALISM FOR THE CHIRAL INTERFACE

In this section, we introduce the Hamiltonian of the chiral interface, including the artificial atoms and the transmission line waveguide. This section is organized as follows: In Sec. **S-IS-I.A** we present a discrete model for the transmission line, which can be conveniently integrated into the waveguide-“giant atom” coupling. In Sec. **S-IS-I.B** we elaborate on the Hamiltonian of the artificial giant atom. In Sec. **S-IS-I.C** we present the way we numerically diagonalize the Hamiltonian of the artificial atom.

### S-I.A. Quantization of the Transmission Line Waveguide

We assume that the transmission line is infinite. In the literature, the one-dimensional continuum of waveguide modes are usually described through a continuous flux field  $\phi(x)$ . The Lagrangian of the waveguide reads

$$L_{tr} = \int_{-\infty}^{\infty} dx \left[ \frac{1}{2} c \dot{\phi}^2 - \frac{1}{2l} (\partial_x \phi)^2 \right]. \quad (\text{S1})$$

where  $c$  and  $l$  are the capacitance and inductance per unit length.

For our purpose it is convenient to describe the waveguide as a discrete series of coupled LC-oscillators. In this model each oscillator has capacitance  $c\delta_z$  and inductance  $l\delta_z$  with  $\delta_z$  an infinitesimal unit length. The coupling capacitor has finite physical length, as illustrated in Fig. **S1**. Since the coupling cannot distinguish modes with wavelengths shorter than this length, it is convenient to define  $\delta_z$  to be this length, so that the variable relevant to the coupling is

$$\bar{\phi}(x_{l/r}) = \frac{1}{\delta_z} \int_{x_{l/r}-\delta_z/2}^{x_{l/r}+\delta_z/2} dx \phi(x). \quad (\text{S2})$$

We then obtain a discrete model:

$$L_{tr} = \sum_{n=-\infty}^{+\infty} \left[ \frac{1}{2} c \delta_z \dot{\phi}_n^2 - \frac{1}{2l\delta_z} (\phi_{n+1} - \phi_n)^2 \right] \quad (\text{S3})$$

The corresponding Hamiltonian is given by

$$H_{tr} = \sum_{n=-\infty}^{\infty} \left[ \frac{1}{2c\delta_z} q_n^2 + \frac{1}{2l\delta_z} (\phi_{n+1} - \phi_n)^2 \right]. \quad (\text{S4})$$

To diagonalize the Hamiltonian, we move to momentum representation:

$$\begin{aligned} \phi_m &= \int_{-\pi}^{\pi} \frac{dk}{2\pi} \phi_k e^{imk} \\ q_m &= \int_{-\pi}^{\pi} \frac{dk}{2\pi} q_k e^{-imk}, \end{aligned} \quad (\text{S5})$$

Since  $[\phi_m, q_n] = i\hbar\delta_{mn}$ , we have  $[\phi_k, q_{k'}] = i\hbar 2\pi\delta(k - k')$ . Note that  $k$  is here defined to be dimensionless. Substituting the above equations into Eq. (S4) and using the equality  $\sum_{n=-\infty}^{\infty} e^{-ikn} = 2\pi\delta(k)$ , we get

$$H_{tr} = \frac{1}{2} \int_{-\pi}^{\pi} \frac{dk}{2\pi} \left( \frac{q_k q_{-k}}{c\delta_z} + 4 \left| \sin \frac{k}{2} \right|^2 \frac{\phi_k \phi_{-k}}{l\delta_z} \right). \quad (\text{S6})$$

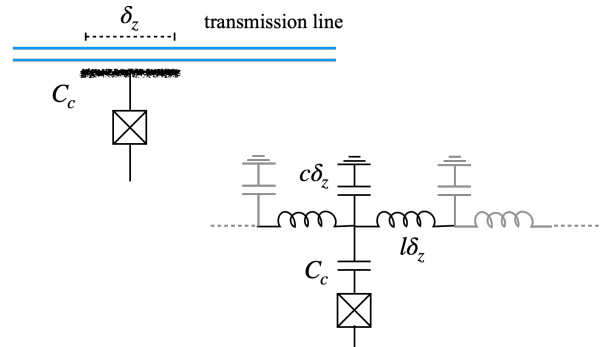


Figure S1. Capacitive coupling to the transmission line. Upper panel: continuous model; Lower panel: discrete model.

Next, we introduce bosonic ladder operators  $b_k$  and  $b_k^\dagger$  satisfying  $[b_k, b_{k'}^\dagger] = 2\pi\delta(k - k')$ , and

$$\phi_k = \sqrt{\frac{\hbar Z_0}{4|\sin(k/2)|}}(b_k + b_{-k}^\dagger), \quad (\text{S7a})$$

$$q_k = i\sqrt{\frac{\hbar|\sin(k/2)|}{Z_0}}(b_k^\dagger - b_{-k}), \quad (\text{S7b})$$

where  $Z_0 = \sqrt{l/c}$  is the impedance. Then the Hamiltonian is diagonalized to  $H_{tr} = \int_{-\pi}^{\pi} \frac{dk}{2\pi} \hbar\omega_k b_k^\dagger b_k$  with

$$\omega_k = \frac{2}{\sqrt{lc}\delta_z} |\sin(k/2)|. \quad (\text{S8})$$

The phase and charge are expressed as

$$\phi_m = \frac{1}{2} \int_{-\pi}^{\pi} \frac{dk}{2\pi} \frac{\sqrt{\hbar Z_0}}{\sqrt{|\sin(k/2)|}} (e^{ikx_m} b_k + e^{-ikx_m} b_k^\dagger), \quad (\text{S9a})$$

$$q_m = i \int_{-\pi}^{\pi} \frac{dk}{2\pi} \sqrt{\frac{\hbar}{Z_0}} \left| \sin \frac{k}{2} \right| (e^{-ikx_m} b_k^\dagger - e^{ikx_m} b_k). \quad (\text{S9b})$$

The two unit cells connected to the “giant atom” will be denoted by “l” and “r”. Their charge number operators  $\hat{n}_{l/r}$  are obtained from the charge operators  $\hat{q}_{a/b}$  via the relation  $\hat{q}_{l/r} = 2e\hat{n}_{l/r}$ .

### S-I.B. Hamiltonian of the Chiral Interface

At first, we consider a cluster composed by the two transmons, the bi-CPB core, and two sections of the transmission line,  $x_l$  and  $x_r$ . The Hamiltonian for these parts reads

$$H_0 = 2e^2 \hat{\mathbf{n}} \mathbf{C}^{-1} \hat{\mathbf{n}} - \sum_{i=a,b} E_{J,i} \cos(\hat{\varphi}_i) - \sum_{j=A,B} E_{Jt,j} \cos(\hat{\varphi}_j) - E_{J,ab} \cos(\hat{\varphi}_a - \hat{\varphi}_b - \varphi_{\text{ext}}) + \frac{1}{2l\delta_z} (\hat{\phi}_l^2 + \hat{\phi}_r^2), \quad (\text{S10})$$

where  $\hat{\mathbf{n}} = (\hat{n}_l, \hat{n}_A, \hat{n}_a - n_{g,a}, \hat{n}_r, \hat{n}_B, \hat{n}_b - n_{g,b})^\top$ . The dimensionless flux used in the Josephson potentials is defined in the form of  $\hat{\varphi} = \hat{\phi} \times 2\pi/\Phi_0$ , and the capacitance matrix is given by

$$\mathbf{C} = \begin{pmatrix} c\delta_z & -C_{c,A} & 0 & 0 & 0 & 0 \\ -C_{c,A} & C_{\Sigma,A} & -C_{q,a} & 0 & 0 & 0 \\ 0 & -C_{q,a} & C_{\Sigma,a} & 0 & 0 & -C_{ab} \\ 0 & 0 & 0 & c\delta_z & -C_{c,B} & 0 \\ 0 & 0 & 0 & -C_{c,B} & C_{\Sigma,B} & -C_{q,b} \\ 0 & 0 & -C_{ab} & 0 & -C_{q,b} & C_{\Sigma,b} \end{pmatrix} \quad (\text{S11})$$

where  $C_{\Sigma,A/B} = C_{c,A/B} + C_{t,A/B} + C_{q,a/b}$  is the total capacitance of transmon-A/B, and  $C_{\Sigma,a/b} = C_{\Sigma,A/B} +$

$C_{q,a/b} + C_{ab}$  is the total capacitance of CPB-a/b. Note that offset charges of the transmons are not included. This is justified because for the low energy excitations, the influence of offset charges is exponentially suppressed if  $E_{Jt}$  is much larger than the transmon charging energy [S2].

$H_0$  can be decomposed into the “system” that consists of transmon-A/B and the bi-CPB core:

$$H_{sys} = 2e^2 \sum_{i,i'=a,b} \mathbf{C}_{i,i'}^{-1} (\hat{n}_i - n_{g,i})(\hat{n}_{i'} - n_{g,i'}) - \sum_{i=a,b} E_{J,i} \cos(\hat{\varphi}_i) - E_{J,ab} \cos(\hat{\varphi}_a - \hat{\varphi}_b - \varphi_{\text{ext}}) + 2e^2 \sum_{j,j'=A,B} \mathbf{C}_{j,j'}^{-1} \hat{n}_j \hat{n}_{j'} - \sum_{j=A,B} E_{Jt,j} \cos(\hat{\varphi}_j) + 4e^2 \sum_{i=a,b} \sum_{j=A,B} \mathbf{C}_{ij}^{-1} \hat{n}_j (\hat{n}_i - n_{g,i}), \quad (\text{S12})$$

where terms in the last line covers Eq. (3) of the main text. The interactions to the two unit cells “l” and “r” of the transmission line:

$$H_{int} = 4e^2 \sum_{\xi=l,r} \sum_{i=a,b} \mathbf{C}_{\xi,i}^{-1} \hat{n}_\xi (\hat{n}_i - n_{g,i}) + 4e^2 \sum_{\xi=l,r} \sum_{j=A,B} \mathbf{C}_{\xi,j}^{-1} \hat{n}_\xi \hat{n}_j. \quad (\text{S13})$$

We neglect the corrections to the charging energy from the two transmission line unit cells, and also neglect their direct interaction (expressed by terms with coefficient  $C_{l,r}^{-1}$ ), which is bridged by the coupled core and transmon system. This means that the transmission line Hamiltonian is  $H_{tr}$  (S4) without corrections other than from the coupling to the excitations of the systems. That is, the total Hamiltonian is written as

$$H = H_{sys} + H_{tr} + H_{int}. \quad (\text{S14})$$

### S-I.C. Hilbert Space Truncation Used in the Numerical Calculations

We numerically diagonalize  $H_{sys}$  (S12) in a truncated Hilbert space

$$\mathcal{H} = \mathcal{H}_A \otimes \mathcal{H}_B \otimes \mathcal{H}_a \otimes \mathcal{H}_b. \quad (\text{S15})$$

Therein,  $\mathcal{H}_A$  is spanned by the lower energy eigenstates of the bare transmon Hamiltonian:

$$H_A = 2e^2 \mathbf{C}_{A,A}^{-1} \hat{n}_A^2 - E_{Jt} \cos(\hat{\varphi}_A) \quad (\text{S16})$$

and similarly for  $\mathcal{H}_B$ . The CPB Hilbert space  $\mathcal{H}_{a/b}$  is spanned by the charge number states, i.e., the eigenstates of  $\hat{n}_{a/b}$  with eigenvalue  $n = -3, -2, \dots, 4$  (the “sweet spot” satisfying  $0.5 < n_{g,a/b} < 1$  is chosen). The dimensions of each space is varied to ensure the convergence of

Dev-1: main text Fig. 3(c)					
$\mathcal{H}_t/\mathcal{H}_{\text{CPB}}$	$\omega_{01}$	$\omega_{02}$	$\omega_{03}$	$\omega_{04}$	$\omega_{05}$
$3^2/10^2$	5.3321	5.6583	6.1254	9.4978	10.8150
$4^2/8^2$	5.3292	5.6640	6.1222	9.4998	10.7921
$4^2/10^2$	5.3292	5.6640	6.1222	9.4998	10.7921
$5^2/12^2$	5.3294	5.6636	6.1224	9.4997	10.7941

Dev-2: Fig. S3(d)					
$\mathcal{H}_t/\mathcal{H}_{\text{CPB}}$	$\omega_{01}$	$\omega_{02}$	$\omega_{03}$	$\omega_{04}$	$\omega_{05}$
$3^2/10^2$	4.8741	5.2474	5.6737	9.1045	9.9481
$4^2/8^2$	4.8744	5.2463	5.6742	9.1033	9.9654
$4^2/10^2$	4.8744	5.2463	5.6742	9.1033	9.9654
$5^2/12^2$	4.8745	5.2462	5.6743	9.1033	9.9621

Table I. Energy levels of the chiral interface (in units of  $h\text{GHz}$ ) calculated with different truncations of the Hilbert space. The column  $\mathcal{H}_t/\mathcal{H}_{\text{CPB}}$  lists the dimensions of the Hilbert spaces of the transmons and the bi-CPB core.

the eigenvalues of the ground and low-excitation eigenvalues. As shown in Tab. I, we find that it is sufficient to take

$$\dim\mathcal{H}_{A/B} = 4, \dim\mathcal{H}_{a/b} = 8. \quad (\text{S17})$$

That is, the numerical diagonalization is implemented in a 1024-dimensional Hilbert space. After the diagonalization, we neglect most of the eigenstates and keep only the lowest four excited states. These states are then substituted into the general formula for the scattering matrix, to be introduced later, to calculate the fidelity of the circulator.

## S-II. EQUIVALENCE BETWEEN THE BI-CPB CORE AND THE JOSEPHSON JUNCTION RING

In Fig. S2 we illustrated the 3-port Josephson ring of Ref. [S1] and the bi-CPB core used in the main text. Here we show the equivalence between them.

We derive the Hamiltonian of the Josephson ring following Ref. [S1]. The total charge of the three CPBs,  $\hat{N} = \hat{n}_a + \hat{n}_b + \hat{n}_c$ , is conserved. Thus, we restrict the description to the subspace spanned by states  $|\psi\rangle$  satisfying  $\langle\psi|\hat{N}|\psi\rangle = N_0$ . In this subspace, we apply the following

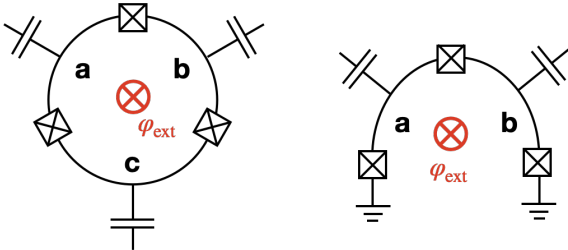


Figure S2. Left panel: 3-port Josephson junction ring; Right panel: 2-port bi-CPB core.

canonical transformations

$$\begin{aligned} \hat{\varphi}_a &= \hat{\varphi}'_a + \hat{\varphi}'_c, \hat{\varphi}_b = \hat{\varphi}'_c - \hat{\varphi}'_b, \hat{\varphi}_c = \hat{\varphi}'_c, \\ \hat{n}_a &= \hat{n}'_a, \hat{n}_b = -\hat{n}'_b, \hat{n}_c = -\hat{n}'_a + \hat{n}'_b + \hat{n}'_c, \end{aligned} \quad (\text{S18})$$

where  $\hat{n}'_c = \hat{N}$  is conserved hence the conjugate variable  $\hat{\varphi}'_c$  is cyclic. Therefore, the Hamiltonian restricted to this subspace has the form

$$\begin{aligned} H_{(N_0)} &= 4E_C \left[ (\hat{n}'_a - n'_{g,a})^2 + (\hat{n}'_b + n'_{g,b})^2 - \hat{n}'_a \hat{n}'_b \right] \\ &\quad - E_J \cos(\hat{\varphi}'_a - \frac{\varphi_{\text{ext}}}{3}) - E_J \cos(\hat{\varphi}'_b - \frac{\varphi_{\text{ext}}}{3}) \\ &\quad - E_J \cos(\hat{\varphi}'_a + \hat{\varphi}'_b + \frac{\varphi_{\text{ext}}}{3}) \end{aligned} \quad (\text{S19})$$

where the junctions are assumed to be identical for convenience,  $n'_{g,a} = \frac{1}{2}(n_{g,a} - n_{g,c} + N_0)$  and  $n'_{g,b} = \frac{1}{2}(n_{g,b} - n_{g,c} + N_0)$ .

Next, we perform the transformations  $\hat{\varphi}'_{a/b} \rightarrow \hat{\varphi}'_{a/b} + \frac{1}{3}\varphi_{\text{ext}}$ , which is then followed by

$$\hat{\varphi}'_b \rightarrow -\hat{\varphi}'_b, \hat{n}'_b \rightarrow -\hat{n}'_b. \quad (\text{S20})$$

With this replacement, the Hamiltonian is brought into the form

$$\begin{aligned} H_{(N_0)} &= 4E_C \left[ (\hat{n}'_a - n'_{g,a})^2 + (\hat{n}'_b - n'_{g,b})^2 + \hat{n}'_a \hat{n}'_b \right] \\ &\quad - E_J \cos(\hat{\varphi}'_a) - E_J \cos(\hat{\varphi}'_b) \\ &\quad - E_J \cos(\hat{\varphi}'_a - \hat{\varphi}'_b + \varphi_{\text{ext}}). \end{aligned} \quad (\text{S21})$$

This is formally equivalent to the Hamiltonian of our bi-CPB with for suitable charging energies and offset charges  $\tilde{n}_{g,a/b}$  given by

$$\begin{aligned} \tilde{n}_{g,a} &= \frac{4}{3}n'_{g,a} - \frac{2}{3}n'_{g,b}, \\ \tilde{n}_{g,b} &= \frac{4}{3}n'_{g,b} - \frac{2}{3}n'_{g,a}. \end{aligned} \quad (\text{S22})$$

## S-III. SINGLE PHOTON SCATTERING MATRIX

Here we derive the scattering matrix for a single incident photon. The formulas derived below will be used to calculate the fidelity of a circulator based on the chiral interfaces with and without the transmons. It will be convenient to expand the operators of the chiral system on eigenstates of its Hamiltonian, which can then be specified on demand. We will apply the rotating-wave approximation to the interaction between the chiral system and the transmission line waveguide (S13). This means that an operator representing the emission of a photon is always associated with a jump from states of higher energy to lower, and vice versa. For simplicity, we also omit the inelastic scattering where a single input photon is scattered into two or more photons of lower frequency.

Thus, we consider only the decay from an excited state to the ground state excluding intermediate lower excited state. This is justified in the discussion section of the main text. In the treatment below we include the Lamb shift caused by coupling to the waveguide but neglect e.g. effects caused by divergences of the high frequency light modes and corrections to the dipole approximation of the

transmon-waveguide coupling. Such effect should be absorbed into the model presented below by renormalizing parameters like energy levels and coupling strengths. A more sophisticated theory which carefully addresses all these effects is beyond of the scope of this work.

Explicitly, the system Hamiltonian is expressed as

$$H/\hbar = \int_{-\pi}^{\pi} \frac{dk}{2\pi} \omega_k b_k^\dagger b_k + \sum_n e_n |\phi_n\rangle \langle \phi_n| + i \sum_{\xi, i; n} \int_{-\pi}^{\pi} \frac{dk}{2\pi} \sqrt{\kappa_{\xi ik}} b_k^\dagger e^{-ikx_\xi} \eta_{in} \sigma_n^- + h.c. \quad (S23)$$

where index  $\xi \in \{l, r\}$ , index  $n$  runs over the numerically obtained excited states  $|\phi_n\rangle$  of  $H_{sys}$  ( $n \leq 4$  in our calculation), index  $i \in \{a, b, A, B\}$ ,  $\sigma_n^- = |g\rangle \langle \phi_n|$  and  $\eta_{in} \equiv \langle g | \hat{n}_i | \phi_n \rangle$  with  $|g\rangle$  the ground state of  $H_{sys}$ . Decay between the excited states are neglected, as explained above. The coupling strength is

$$\sqrt{\kappa_{\xi ik}} = 2eC_{\xi, i}^{-1} \sqrt{\frac{|\sin(k/2)|}{\hbar Z_0}}. \quad (S24)$$

To describe a situation where a single photon is incident, we consider the single-excitation ansatz

$$|\Psi\rangle = \sum_n c_n |\phi_n\rangle + \int_{-\pi}^{\pi} \frac{dk}{2\pi} f_k b_k^\dagger |g, \emptyset\rangle, \quad (S25)$$

where  $|\emptyset\rangle$  is the vacuum of the waveguide photon. Then the Schrödinger equation leads to

$$i\partial_t c_n = c_n e_n - i \int_{-\pi}^{\pi} \frac{dk}{2\pi} f_k \sum_{\xi, i} e^{ikx_\xi} \sqrt{\kappa_{\xi ik}} \eta_{in}^*, \quad (S26a)$$

$$i\partial_t f_k = \omega_k f_k + i \sum_{\xi, i, n} c_n e^{-ikx_\xi} \sqrt{\kappa_{\xi ik}} \eta_{in}. \quad (S26b)$$

The second equation is formally solved in two ways

$$f_k(t) = f_k(t_0) e^{-i\omega_k(t-t_0)} + \sum_{\xi, i, n} e^{-ikx_\xi} \sqrt{\kappa_{\xi ik}} \eta_{in} \int_{t_0}^t d\tau e^{-i\omega_k(t-\tau)} c_n(\tau), \quad (S27a)$$

and

$$f_k(t) = f_k(t_f) e^{-i\omega_k(t-t_f)} + \sum_{\xi, i, n} e^{-ikx_\xi} \sqrt{\kappa_{\xi ik}} \eta_{in} \int_{t_f}^t d\tau e^{-i\omega_k(t-\tau)} c_n(\tau). \quad (S27b)$$

Therein, the input and output fields are defined as  $f_k^{in}(t) = f_k(t_0) e^{-i\omega_k(t-t_0)}$  and  $f_k^{out}(t) = f_k(t_f) e^{i\omega_k(t_f-t)}$ , respectively. In Fourier space (assuming  $t_f - t_0 = \infty$ ) we then obtain the input-output relation

$$F_k^{out}(\omega) - F_k^{in}(\omega) = 2\pi\delta(\omega - \omega_k) \sum_{\xi, i, n} e^{-ikx_\xi} \sqrt{\kappa_{\xi ik}} \eta_{in} C_n(\omega). \quad (S28)$$

We substitute the input field solution Eq. (S27a) into Eq. (S26a) and obtain

$$(i\partial_t - e_n) c_n = -i \int_{-\pi}^{\pi} \frac{dk}{2\pi} \sum_{\xi, i} e^{ikx_\xi} \sqrt{\kappa_{\xi ik}} \eta_{in}^* f_k^{in}(t) - i \sum_{\xi, i' i'' n'} \int_{-\pi}^{\pi} \frac{dk}{2\pi} e^{ik(x_\xi - x_{\xi'})} \sqrt{\kappa_{\xi ik} \kappa_{\xi' i'' k}} \eta_{in}^* \eta_{i' n'} \int_{t_0}^t d\tau e^{-i\omega_k(t-\tau)} c_{n'}(\tau). \quad (S29)$$

The integral of  $\tau$  is evaluated as (assuming  $t - t_0 \rightarrow \infty$ )

$$\int_{t_0}^t d\tau e^{-i(\omega_k - \omega_0)(t-\tau)} \tilde{c}_{n'}(\tau) e^{-i\omega_0(t-t_0)} \approx c_{n'}(t) \frac{i}{\omega_0 - \omega_k + i0^+}. \quad (S30)$$

The fast evolution part of  $c_{n'}(t)$  is determined by the input frequency  $\omega_0$ . The term  $\sqrt{\kappa_{\xi ik}\kappa_{\xi' i' k}}$  contributes a factor of  $|\sin(k/2)|$ . Then the integral over  $k > 0$  is approximated by defining  $q = k - k_0$  and extending the range of integral over  $q$  to infinity

$$e^{ik_0(x_\xi - x_{\xi'})} \left| \sin \frac{k_0}{2} \right| \int_{-\infty}^{\infty} \frac{dq}{2\pi} e^{iq(x_\xi - x_{\xi'})} \left( \mathcal{P} \frac{-i}{v_g q} + \pi \delta(v_g q) \right). \quad (\text{S31})$$

For the principal integral, we substitute  $e^{iq\Delta x} = \cos(q\Delta x) + i\sin(q\Delta x)$  and notice that terms of cosine vanish and those of sine can be solved by  $\int_{-\infty}^{\infty} dx \frac{\sin x}{x} = \pi$ . That is, the integral over  $q$  of Eq. (S31) vanishes if  $x_\xi - x_{\xi'} < 0$ , equals  $\frac{1}{v_g}$  if  $x_\xi - x_{\xi'} > 0$ , and equals  $\frac{1}{2v_g}$  if  $x_\xi = x_{\xi'}$ . As to the integral of  $k < 0$ , it is approximated by, defining  $k = -k_0 + q$ ,

$$e^{-ik_0(x_\xi - x_{\xi'})} \left| \sin \frac{k_0}{2} \right| \int_{-\infty}^{\infty} \frac{dq}{2\pi} e^{iq(x_\xi - x_{\xi'})} \left( \mathcal{P} \frac{i}{v_g q} + \pi \delta(v_g q) \right). \quad (\text{S32})$$

Similarly, now it vanishes if  $x_\xi - x_{\xi'} > 0$ , equals  $\frac{1}{v_g}$  if  $x_\xi - x_{\xi'} < 0$ , and equals  $\frac{1}{2v_g}$  if  $x_\xi = x_{\xi'}$ . Then we take it into the integral over  $k$  and obtain

$$\int_{-\pi}^{\pi} \frac{dk}{2\pi} e^{ik(x_\xi - x_{\xi'})} \frac{i|\sin(k/2)|}{\omega_0 - \omega_k + i0^+} \approx v_g^{-1} \left| \sin \frac{k_0}{2} \right| e^{ik_0|x_\xi - x_{\xi'}|} \quad (\text{S33})$$

where  $k_0 = \omega_0/v_g > 0$ . It leads to

$$(i\partial_t - e_n)c_n = -i \int_{-\pi}^{\pi} \frac{dk}{2\pi} \sum_{\xi, i} e^{ikx_\xi} \sqrt{\kappa_{\xi ik}} \eta_{in}^* f_k^{in}(t) - i \sum_{\xi \xi' ii' n'} \frac{\sqrt{\kappa_{\xi ik_0} \kappa_{\xi' i' k_0}}}{v_g} \eta_{in}^* \eta_{i'n'} e^{ik_0|x_\xi - x_{\xi'}|} c_{n'}. \quad (\text{S34})$$

In the Fourier space, it is expressed as

$$C_n(\omega) = -i \int_{-\pi}^{\pi} \frac{dk}{2\pi} \left[ \omega \mathbb{I} - \hat{E} + i\Sigma \right]_{nm}^{-1} \alpha_m(k) F_k^{in}(\omega) \quad (\text{S35})$$

where  $\hat{E}_{nm} = e_n \delta_{n,m}$  and

$$\alpha_m(k) = \sum_{\xi, i} e^{ikx_\xi} \sqrt{\kappa_{\xi ik}} \eta_{im}^* \quad (\text{S36a})$$

$$\Sigma_{n,m} = \frac{1}{v_g} \sum_{\xi \xi' ii'} \sqrt{\kappa_{\xi ik_0} \kappa_{\xi' i' k_0}} e^{ik_0|x_\xi - x_{\xi'}|} \eta_{in}^* \eta_{i'm}. \quad (\text{S36b})$$

Substituting it into Eq. (S28), we get

$$F_{k_0}^{out} - F_{k_0}^{in} = -i \frac{1}{v_g} \sum_{m,n} \alpha_n^*(k_0) \left[ \omega_{k_0} \mathbb{I} - \hat{E} + i\Sigma \right]_{nm}^{-1} [\alpha_m(k_0) F_{k_0}^{in} + \alpha_m(-k_0) F_{-k_0}^{in}] \quad (\text{S37})$$

This leads to the scattering matrix

$$\begin{pmatrix} F_{k_0}^{out} \\ F_{-k_0}^{out} \end{pmatrix} = \begin{pmatrix} 1 - \frac{i}{v_g} \alpha_n^*(k_0) [(\omega_{k_0} - e_n) \mathbb{I} + i\Sigma]_{nm}^{-1} \alpha_m(k_0) & -\frac{i}{v_g} \alpha_n^*(k_0) [(\omega_{k_0} - e_n) \mathbb{I} + i\Sigma]_{nm}^{-1} \alpha_m(-k_0) \\ -\frac{i}{v_g} \alpha_n^*(-k_0) [(\omega_{k_0} - e_n) \mathbb{I} + i\Sigma]_{nm}^{-1} \alpha_m(k_0) & 1 - \frac{i}{v_g} \alpha_n^*(-k_0) [(\omega_{k_0} - e_n) \mathbb{I} + i\Sigma]_{nm}^{-1} \alpha_m(-k_0) \end{pmatrix} \begin{pmatrix} F_{k_0}^{in} \\ F_{-k_0}^{in} \end{pmatrix}. \quad (\text{S38})$$

In the evaluation of the scattering matrix, the coupling strengths are related to the physical parameters accord-

ing to the relation

$$\frac{\sqrt{\kappa_{\xi ik} \kappa_{\xi' i' k}}}{v_g} = (2ec\delta_z)^2 C_{\xi, i}^{-1} C_{\xi', i'}^{-1} \frac{1}{2\hbar} Z_0 \omega_k. \quad (\text{S39})$$

The fidelity of the circulator can be evaluated by substituting the matrix elements of Eq. (S38) into Eq. (2) of the main text.

#### S-IV. ADDITIONAL RESULTS FOR LEVEL STABILITY AND DEVICE TUNABILITY

In the main text, the numerical results are obtained for rather symmetric device parameters, that is, the capacitors used in the bi-CPB core are assumed to have identical capacitance, and  $k_0d$  and  $\varphi_{\text{ext}}$  are both taken to be  $0.5\pi$ . To demonstrate that all these precise choices are not essential, we here present parallel calculations for another family of device parameters.

Results are plotted in Fig. S3 for the device parameters listed in Fig. S3(d). These plots are equivalent to those presented in the main text, and they convey the same message. Our optimization only aims at achieving  $\max_{\omega} F_R(\omega) > 0.99$ . Thus the adapted parameters shown in the lower panel of Fig. S3(c) are not unique.

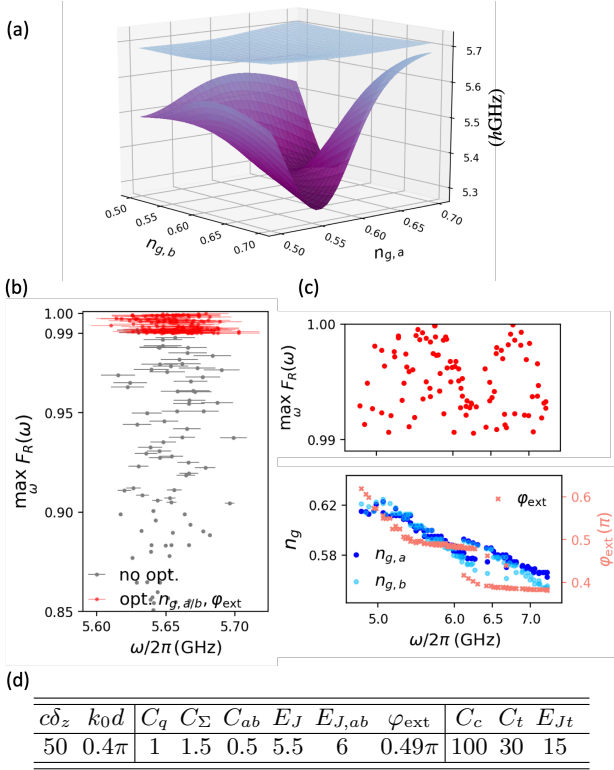


Figure S3. Results parallel to the main text but different device parameters. (a) The energy levels  $\omega_{01}$  and  $\omega_{02}$  as a function of offset charges  $n_{g,a(b)}$ . (b) 150 samplings of fabrication variations. (c) 100 examples of fidelity of chirality obtained by tuning transmon Josephson energies. (d) Device parameters. Units for the capacitances and the Josephson energies are fF and hGHz, respectively.

#### S-V. DEPENDENCE OF FIDELITY AND BANDWIDTH ON THE CPB OFFSET CHARGES AND THE EXTERNAL FLUX

In the main text, we have shown that fabrication variations can be addressed by tuning the offset charges  $n_{g,a/b}$  and the external flux  $\varphi_{\text{ext}}$ , but have not gone into details about the optimized values of them. Since the fabrication variations for capacitance ( $\pm 1\%$ ) is smaller than that of Josephson energies ( $\pm 10\%$ ), we focus on only the latter and elaborate on a few examples of extreme variations.

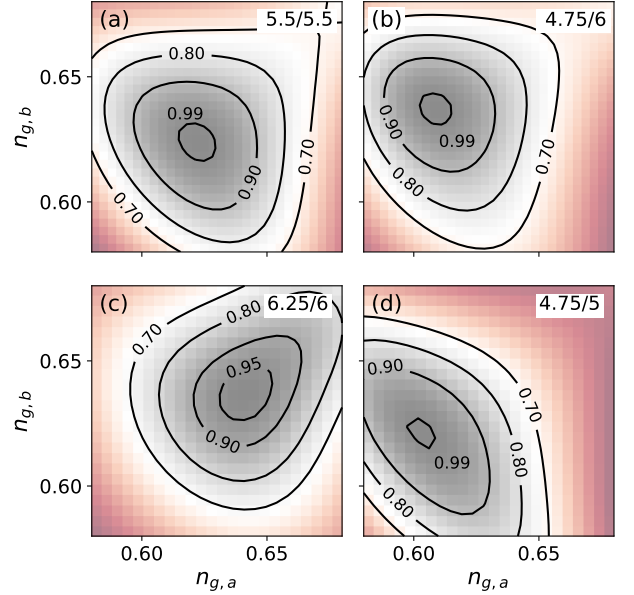


Figure S4. Maximal fidelity as a function of  $n_{g,a}$  and  $n_{g,b}$  for different values of  $E_{J,a}/E_{J,b}$  labelled in the upper right corner of each sub-figure (in units of hGHz). The other device parameters are the same as in Fig. 3(c) of the main text.

We use the device parameters listed in Fig. 3(c) of the main text, where  $E_{J,ab} = 5$  hGHz and  $E_{J,a} = E_{J,b} = 5.5$  hGHz. We consider three cases where  $E_{J,a}/E_{J,b}$  deviate from the intended values significantly: one is smaller while the other is larger, both are larger, or both are smaller, than the intended values. The peak fidelity of the intended case and three examples of extreme fabrication variation are plotted in Fig. S4 as a function of  $n_{g,a}$  and  $n_{g,b}$ , with  $\varphi_{\text{ext}}$  fixed at  $0.5\pi$ . It shows that by adjusting only the offset charges, the fabrication variations of Fig. S4(b) and S4(d) can be addressed. In Fig. S4(c) the maximal fidelity cannot be lifted beyond 0.99. In this case, the external magnetic flux  $\varphi_{\text{ext}}$  must be tuned as well. We obtained  $\max_{\omega} F_R = 0.996$  with parameters  $n_{g,a} = 0.63$ ,  $n_{g,b} = 0.631$  and  $\varphi_{\text{ext}} = 0.534\pi$ .

Next, we study how the bandwidth and peak fidelity depend on  $n_{g,a/b}$  and  $\varphi_{\text{ext}}$ . For convenience, we assume  $n_{g,a} = n_{g,b} = n_g$  and plot the results in Fig. S5 for the device parameters used in the main text, and those listed in Fig. S3(d). From Fig. S4 and S5 we can see that to stabilize the performance of the chiral interface, the

offset charges  $n_{g,a/b}$  and fluxes should be controlled at the percent level.

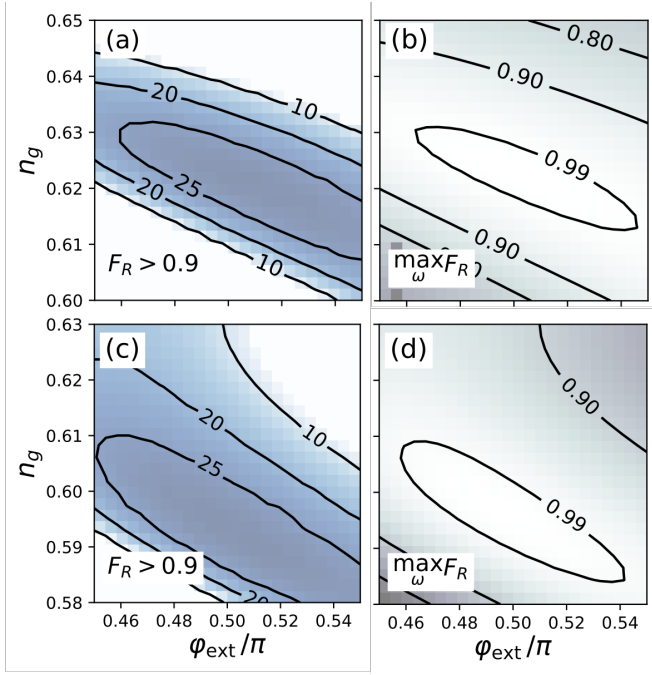


Figure S5. Dependence of the bandwidth for  $F_R > 0.9$  (a,c, in units of MHz) and maximal fidelity  $\max_{\omega} F_R(\omega)$  (b,d) on the offset charge and external flux. The device parameters are: (a,b) parameter listed in the main text Fig. 3(c); (c,d) parameter listed in Fig. S3(d).

[S1] J. Koch, A. A. Houck, K. L. Hur, and S. M. Girvin, Time-reversal-symmetry breaking in circuit-qed-based photon lattices, *Physical Review A* **82**, [10.1103/physreva.82.043811](#) (2010).

[S2] J. Koch, T. M. Yu, J. Gambetta, A. A. Houck, D. I. Schuster, J. Majer, A. Blais, M. H. Devoret, S. M. Girvin, and R. J. Schoelkopf, Charge-insensitive qubit design derived from the cooper pair box, *Phys. Rev. A* **76**, 042319 (2007).